Correlation effects in two-dimensional MX_2 and MA_2Z_4 (M = Nb, Ta; X = S, Se, Te; A = Si, Ge; Z = N, P) cold metals: Implications for device applications

W. Beida [1,2] E. Şaşıoğlu [3,*] M. Tas [4] C. Friedrich [1] S. Blügel [1] I. Mertig [3] and I. Galanakis [5,†]

[1]Peter Grünberg Institut, Forschungszentrum Jülich, 52425 Jülich, Germany
[2]Physics Department, RWTH Aachen University, 52062 Aachen, Germany
[3]Institute of Physics, Martin Luther University Halle-Wittenberg, 06120 Halle (Saale), Germany
[4]Department of Physics, Gebze Technical University, 41400 Kocaeli, Turkey
[5]Department of Materials Science, School of Natural Sciences, University of Patras, GR-26504 Patra, Greece

(Received 20 November 2024; revised 20 December 2024; accepted 9 January 2025; published 24 January 2025)

Cold metals, characterized by their distinctive band structures, hold promise for innovative electronic devices such as tunnel diodes with negative differential resistance (NDR) effect and field-effect transistors (FETs) with sub-60 mV/dec subthreshold swing (SS). In this study, we employ the *GW* approximation and HSE06 hybrid functional to investigate the correlation effects on the electronic band structure of two-dimensional cold metallic materials, specifically focusing on MX_2 and MA_2Z_4 (M = Nb, Ta; X = S, Se, Te; A = Si, Ge; Z = N, P) compounds in 1H structure. These materials exhibit a unique band structure with an isolated metallic band around the Fermi energy, denoted as W_m, as well as two energy gaps: the internal gap E_g^I below the Fermi level and the external gap E_g^E above the Fermi level. These three electronic structure parameters play a decisive role in determining the current-voltage (I-V) characteristics of tunnel diodes, the nature of the NDR effect, and the transfer characteristics and SS value of FETs. Our calculations reveal that both *GW* and HSE06 methods yield consistent electronic structure properties for all studied compounds. We observed a consistent increase in both internal and external band gaps, as well as metallic bandwidths, across all pn-type cold metal systems. Notably, the internal band gap E_g^I exhibits the most substantial enhancement, highlighting the sensitivity of these materials to correlation effects. In contrast, the changes in the metallic bandwidth W_m and external band gap E_g^E are relatively modest. These findings offer valuable insights for designing and optimizing cold metal-based devices. Materials like $NbSi_2N_4$, $NbGe_2N_4$, and $TaSi_2N_4$ show particular promise for high-performance NDR tunnel diodes and sub-60 mV/dec SS FETs.

DOI: 10.1103/PhysRevMaterials.9.014006

I. INTRODUCTION

The experimental discovery of graphene through the exfoliation of graphite has sparked an unprecedented surge of interest in two-dimensional (2D) materials [1]. The reduced dimensionality of 2D materials compared to bulk materials gives rise to unique quantum size effects, leading to novel physical and chemical properties [1]. In particular, the confinement of electronic and optical properties within a 2D plane has opened up exciting possibilities for a wide range of technological applications. Among 2D materials, semiconductors such as transition metal dichalcogenides (TMDCs), including MoS_2 and WS_2, have garnered significant attention for their potential in next-generation electronic and optoelectronic devices [2]. Furthermore, 2D semiconductors are expected to play a crucial role in emerging technologies like valleytronics, spintronics, and energy harvesting, pushing the boundaries of modern semiconductor technology [3–5].

Despite the promise of 2D semiconductors like TMDCs, the search for novel materials with exceptional electronic properties remains critical. Among these materials, "cold metals" have emerged as a class with distinctive electronic structures and functionalities [6]. These materials are characterized by their unconventional band structures, which deviate significantly from traditional metals and semiconductors. As shown in Fig. 1, cold metals exhibit unique densities of states (DOS), featuring well-defined internal (E_g^I) and external (E_g^E) band gaps, along with a metallic band width (W_m) that govern their electronic properties. Depending on the position of the Fermi level, cold metals can be classified into three types: p-type, n-type, and pn-type. In p-type and n-type cold metals, the Fermi level intersects the valence or conduction bands, respectively, resulting in intrinsic conductivity without the need for doping. Of particular interest are pn-type cold metals, which feature an isolated metallic band near the Fermi level, flanked by energy gaps, distinguishing them from conventional materials. In the literature, p- and n-type cold metals are also referred to as "gapped metals" [7–9].

Cold metals have already been investigated for a wide range of applications, from thermoelectrics and plasmonics to nanoelectronics and spintronics. In plasmonics, cold metals present an innovative solution to the issue of optical losses [10–15]. Traditional metals experience significant energy dissipation due to electronic transitions, limiting the performance

*Contact author: ersoy.sasioglu@physik.uni-halle.de
†Contact author: galanakis@upatras.gr

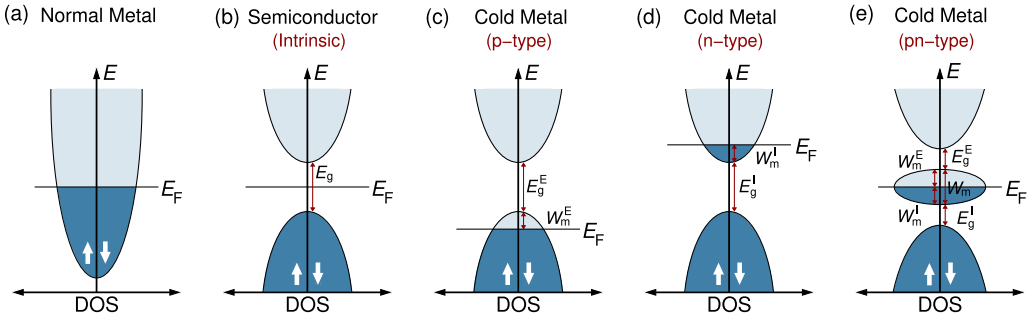

FIG. 1. Schematic representation of the density of states (DOS) depicting: (a) a normal metal, (b) a semiconductor, (c) a p-type cold metal, (d) an n-type cold metal, and (e) a pn-type cold metal. The symbols E_g, E_g^I, and E_g^E corresponds to the band gap of the semiconductor, as well as the internal and external band gaps of cold metal, respectively. The width of the metallic band for the cold metal is designated by W_m. The Fermi level is denoted by E_F. For p- and n-type cold metals the distance between E_F and the valence band maximum and conduction band minimum are denoted by W_m^E and W_m^I, respectively.

of plasmonic devices. In contrast, cold metals, with their reduced density of states for scattering in the near-infrared region and the presence of energy gaps, provide an efficient alternative by suppressing optical losses. This low-energy dissipation enables the design of high-performance plasmonic devices [16]. Moreover, cold metals show great potential in thermoelectric applications due to their unique electronic structure [7]. Unlike conventional metals, which exhibit a relatively constant density of states near the Fermi level, cold metals display a sharp decrease in the density of states around the partial energy gap. This leads to an enhanced Seebeck coefficient, a key factor in efficient thermoelectric conversion. Combined with their high electrical conductivity, cold metals offer an optimized balance, positioning them as strong candidates for advanced thermoelectric materials.

While cold metals hold significant promise in thermoelectric and plasmonic applications, their potential in nanoelectronics is equally compelling. These materials enable innovative device concepts such as steep-slope field-effect transistors (FETs) and negative differential resistance (NDR) tunnel diodes with ultrahigh peak-to-valley current ratios (PVCR) [17–19]. By harnessing the unique electronic properties of cold metals, these devices could outperform conventional semiconductor technologies, potentially leading to more energy-efficient electronics.

II. MOTIVATION AND AIM

One of the key advantages of cold metals in nanoelectronics lies in their lack of band tails, a common issue in traditional p- and n-type semiconductors caused by doping and fluctuations in doping concentrations. Band tails have been extensively studied and are known to degrade the performance of devices such as tunnel FETs and Esaki tunnel diodes [20–26]. In tunnel FETs, band tails increase the subthreshold slope (SS), while in Esaki diodes, they reduce the PVCR. Cold metals, by contrast, are free of band tails, providing an inherent advantage in the design of advanced nanoelectronic devices, such as steep-slope transistors and NDR tunnel diodes [27].

Cold metals are theoretically proposed to overcome the thermionic limit of 60 mV/decade SS in traditional FETs, which limits the reduction of power consumption while maintaining switching speed [28]. The primary challenge in conventional transistors is the presence of high-energy hot electrons that contribute to this limit. In experimental studies, graphene has been demonstrated as a potential solution due to its ability to suppress high-energy electrons, thanks to its unique band structure [29,30]. However, recent theoretical works suggest that cold metals offer an even better alternative than graphene [10,28]. Their intrinsic band gaps above the Fermi level act as energy filters for high-energy hot electrons, selectively allowing only low-energy cold electrons to participate in transport. This energy filtering mechanism could enable sub-60 mV/dec switching, significantly improving energy efficiency by reducing leakage currents and sharpening the switching curve. As a result, cold-metal-based FETs are projected to achieve faster switching at lower operating voltages, making them suitable for future energy-efficient computing systems.

In Fig. 2(a), we present the schematic transfer characteristics of an FET utilizing cold metal source and drain electrodes, comparing it with a conventional MOSFET. The cold metal FET demonstrates a steeper subthreshold slope due to the energy filtering effect from the band gaps in cold metals. This comparison illustrates the potential of cold metal FETs to achieve better energy efficiency and sharper switching behavior than traditional MOSFETs, which are constrained by the thermionic limit. The theoretical promise of cold metals in FETs is supported by ab-initio simulations based on density functional theory (DFT). Simulations of cold-metal FETs using 2D materials like $NbSe_2$ and $NbTe_2$ have demonstrated subthreshold slopes below 60 mV/decade at room temperature [18,27,28]. Additionally, these simulations show an NDR effect with ultrahigh PVCR values, further emphasizing the potential of cold metals in electronic device applications [17,18,27]. While graphene-based transistors have already been experimentally demonstrated, cold metals offer a pathway to even more efficient steep-slope transistors. In addition to FETs, cold metals show potential in NDR tunnel diodes. By selecting appropriate pn-type cold metal electrodes, the tunnel diode can exhibit either an N-type (NbS_2/h-BN/NbS_2) or Λ-type (AlI_2/MgI_2/AlI_2 NDR effect [17]. In Fig. 2(b), we present schematic *I-V* characteristics of a cold metal tunnel diode, highlighting the sharpness of the N-type NDR effect compared to a conventional Esaki diode.

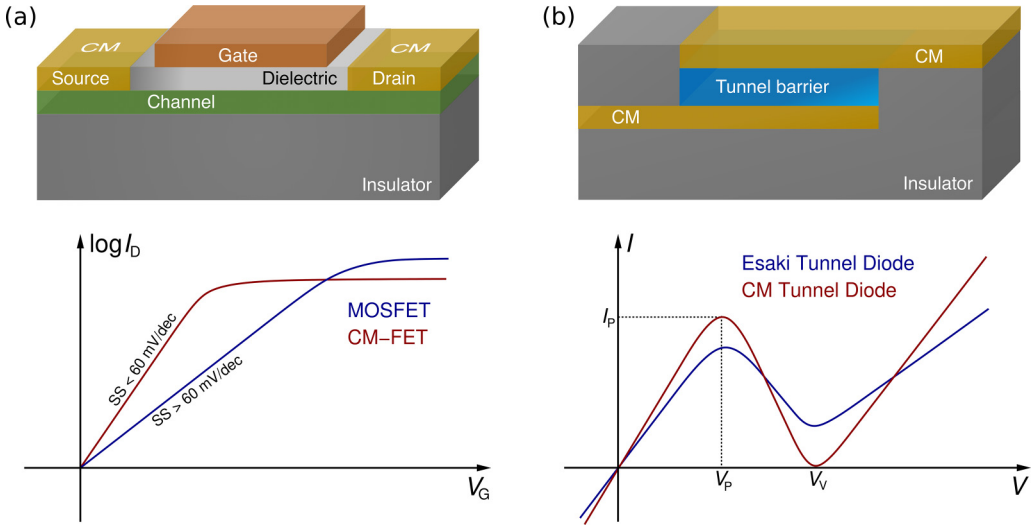

FIG. 2. (a) Schematic illustration of a two-dimensional vertical field-effect transistor (FET) utilizing cold metal (CM) electrodes, along with its transfer characteristics, including a comparison with a conventional MOSFET. The subthreshold slope (SS) is indicated. (b) Schematic illustration of a two-dimensional vertical negative differential resistance (NDR) tunnel diode based on cold metals, accompanied by its current-voltage (I-V) characteristics, with a comparison to the I-V curves of an Esaki tunnel diode.

Given the promising potential of cold metals in nanoelectronic devices, this study aims to investigate the effect of electronic correlations on their electronic band structures. By employing the state-of-the-art GW approximation and HSE06 hybrid functional, we explore changes in the internal (E_g^I) and external (E_g^E) band gaps, as well as the metallic bandwidth (W_m), in MX_2 and MA_2Z_4 (M = Nb, Ta; X = S, Se, Te; A = Si, Ge; Z = N, P) compounds in the 1H structure. These electronic structure parameters are crucial for understanding the performance of cold metal-based tunnel diodes and FETs. Our study focuses on how these parameters vary across different material compositions and the influence of correlation effects. By understanding how these correlation effects impact the electronic properties, we aim to offer insights into the design and optimization of cold metal-based devices, such as steep-slope transistors and NDR tunnel diodes, contributing to the development of next-generation, energy-efficient nanoelectronics.

III. COMPUTATIONAL METHODS

A. Crystal structure

The MX_2 and MA_2Z_4 compounds studied in this work crystallize in the 1H structure, a common phase for TMDCs. The 1H structure consists of layers of transition metal atoms (M) sandwiched between layers of chalcogenide (X) or pnictogen (A, Z) atoms. Figure 3 illustrates the crystal structure of these compounds. MX_2 compounds have been experimentally synthesized in both 1H and 1T structures [31,32]. However, for this study, we focus on the 1H structure because it exhibits cold metallic behavior and is the most stable phase, while the 1T structure displays normal metallic characteristics. The MA_2Z_4 compounds, proposed in Ref. [33], are a new family of van der Waals layered materials. These compounds consist of a MZ_2 layer intercalated between two AZ monolayers, as shown in Fig. 3(b). Some members of this family, such as $MoSi_2N_4$, were experimentally synthesized before theoretical studies [34]. This initial computational study led to the prediction of 72 thermodynamically and dynamically stable MA_2Z_4 compounds [33]. For our calculations, we included six compounds from Ref. [33] which are cold metals: $(Nb,Ta)(Si,Ge)_2N_4$ and $(Nb,Ta)Si_2P_4$. The lattice constants are taken from the Computational 2D Materials Database (C2DB) for the MX_2 compounds [35–37] while for the MA_2Z_4 compounds the lattice constants were taken from Ref. [33] and are presented in Table I.

B. Computational details

To investigate the electronic band structures of the MX_2 and MA_2Z_4 compounds, we employed two first-principles electronic structure methods. The first approach utilized the QUANTUMATK software package [38,39], which implements both linear combinations of atomic orbitals (LCAO) and Plane Waves (PW) as the basis sets along with norm-conserving PseudoDojo pseudopotentials [40]. We initially employed the Perdew-Burke-Ernzerhof (PBE) parametrization of the generalized-gradient approximation (GGA) for exchange-correlation energy [41], a standard functional in materials simulations. For improved accuracy in describing exchange interactions, we also applied the Heyd–Scuseria–Ernzerhof (HSE06) hybrid functional [42,43], which mixes exact short-range Hartree-Fock exchange with long-range GGA exchange. While hybrid functionals like HSE06 are particularly suited for improving band gap predictions, their predefined mixing coefficients may not be universally optimal across all material systems. Nevertheless, given the long-range nature of Coulomb interactions in 2D cold metals [44], HSE06 provides an appropriate level of accuracy for capturing the electronic properties of these materials. To simulate the 2D monolayer limit, a vacuum region of 25 Å was added in the 1H structure unit cell to prevent inter-layer interactions, and a

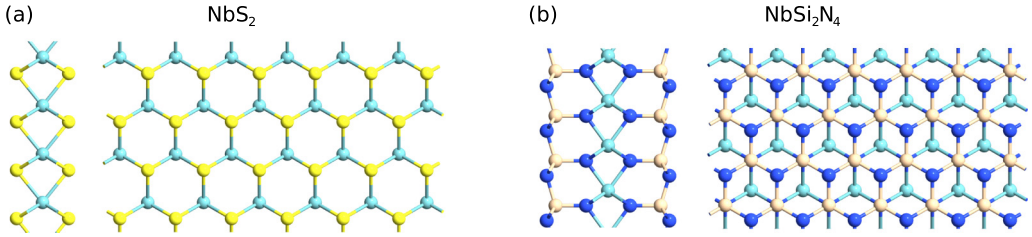

FIG. 3. Side and top views of the two-dimensional crystal structure of monolayer 1H (a) NbS_2 and (b) $NbSi_2N_4$. Both materials exhibit a hexagonal lattice, with each layer consisting of a transition metal (Nb) sandwiched between two chalcogen (S) atoms in NbS_2, or between pnictogen atoms (Si, N) in $NbSi_2N_4$. The 1H phase is characterized by its trigonal prismatic coordination of the transition metal atom.

$18 \times 18 \times 1$ Monkhorst-Pack k-point grid [45] was employed in all self-consistent calculations.

To capture correlation effects more accurately, we performed many-body perturbation theory calculations within the *GW* approximation. Ground-state properties were first computed using the full-potential linearized augmented-plane-wave (FLAPW) method implemented in the FLEUR code [46], using PBE for exchange and correlation. Angular momentum and plane-wave cutoff parameters were set to $l_{\max} = 8$ inside muffin-tin spheres and $k_{\max} = 4.5$ bohr^{-1} in the interstitial region. The Brillouin zone was sampled using an $18 \times 18 \times 1$ **k**-point grid.

Subsequently, one-shot *GW* calculations were performed using the SPEX code [47,48]. In this approach, the off-diagonal elements in the self-energy operator $\Sigma_\sigma(E_{n\mathbf{k}\sigma})$ were neglected, and the expectation values of the local exchange-correlation potential V_σ^{XC} were subtracted to avoid double-counting. The Kohn-Sham (KS) single-particle wavefunctions $\varphi_{n\mathbf{k}\sigma}^{\mathrm{KS}}$ were treated as approximations to quasiparticle (QP) wavefunctions. Hence, the QP energies $E_{n\mathbf{k}\sigma}$ were computed as a first-order perturbation correction to the KS values $E_{n\mathbf{k}\sigma}^{\mathrm{KS}}$ as $E_{n\mathbf{k}\sigma} = E_{n\mathbf{k}\sigma}^{\mathrm{KS}} + \langle\varphi_{n\mathbf{k}\sigma}^{\mathrm{KS}}|\Sigma_\sigma(E_{n\mathbf{k}\sigma}) - V_\sigma^{\mathrm{XC}}|\varphi_{n\mathbf{k}\sigma}^{\mathrm{KS}}\rangle$, where n, $\mathbf{k}$, and σ represent the band index, Bloch vector, and electron spin, respectively. The dynamically screened Coulomb interaction W was expanded using a mixed product basis set, with contributions from both the local atom-centered muffin-tin spheres and plane waves in the interstitial region [49]. The cutoff parameters for the mixed product basis were set to $L_{\max} = 4$ and $G_{\max} = 4$ bohr^{-1}. A consistent computational cell and k-point grid ($18 \times 18 \times 1$) were used across all codes. Relativistic corrections were treated at the scalar-relativistic level for the valence states, while the core states were calculated using the full Dirac equation.

IV. RESULTS AND DISCUSSION

We study two families of 2D compounds in the 1H structure: transition metal dichalcogenides (TMDCs) (Nb, Ta)(S, Se, Te)$_2$ and layered compounds (Nb, Ta)(Si, Ge)$_2$(N, P)$_4$. Table I presents the cold metal character for each compound, alongside the widths of the internal and external energy gaps and the metallic bandwidth, as calculated using the PBE and HSE06 functionals, as well as the *GW* approximation.

The choice of the HSE06 functional and *GW* approximation is supported by prior studies on similar cold metals and TMDCs. For instance, $SrVO_3$ is a well-studied n-type cold

TABLE I. Lattice constants, cold metal type according to the *GW*-based calculations, internal energy gap $E_{\mathrm{g}}^{\mathrm{I}}$, external energy gap $E_{\mathrm{g}}^{\mathrm{E}}$, and metallic bandwidth W_{m} (see Fig. 1 for the definitions) using both FLEUR and QUANTUMATK codes in conjunction with the PBE and HSE06 functionals as well as the *GW* approximation. For the QUANTUMATK code we present both the values obtained using the LCAO and the PW basis sets (the latter in parenthesis). Lattice constants for MX_2 compounds are taken from the Computational 2D Materials Database (C2DB) [35–37], while those for MA_2Z_4 compounds are from Ref. [33].

			FLEUR/SPEX						QUANTUMATK					
Comp.	a_0	CM	$E_{\mathrm{g}}^{\mathrm{I}}$(eV)		$E_{\mathrm{g}}^{\mathrm{E}}$(eV)		W_{m}(eV)		$E_{\mathrm{g}}^{\mathrm{I}}$(eV)		$E_{\mathrm{g}}^{\mathrm{E}}$(eV)		W_{m}(eV)	
	(Å)	Type	*GW*	PBE	*GW*	PBE	*GW*	PBE	HSE06	PBE	HSE06	PBE	HSE06	PBE
NbS_2	3.35	pn	0.95	0.57	1.42	1.21	1.50	1.19	0.84 (0.86)	0.45 (0.46)	1.27 (1.29)	1.15 (1.17)	1.61 (1.60)	1.24 (1.21)
$NbSe_2$	3.47	pn	0.72	0.34	1.59	1.42	1.24	0.90	0.69 (0.63)	0.30 (0.30)	1.40 (1.49)	1.28 (1.33)	1.33 (1.31)	0.98 (0.95)
$NbTe_2$	3.70	p	0.00	0.00	1.21	1.13	1.55	0.91	0.21 (0.14)	0.00 (0.00)	1.42 (1.38)	1.16 (1.14)	1.13 (1.22)	0.92 (0.94)
TaS_2	3.34	pn	1.22	0.67	1.59	1.35	1.78	1.40	0.98 (0.99)	0.57 (0.58)	1.39 (1.42)	1.28 (1.31)	1.89 (1.83)	1.45 (1.41)
$TaSe_2$	3.47	pn	0.49	0.38	1.70	1.47	1.47	1.11	0.84 (0.72)	0.43 (0.39)	1.49 (1.53)	1.38 (1.40)	1.55 (1.52)	1.14 (1.14)
$TaTe_2$	3.71	pn	0.16	0.08	1.22	1.03	1.43	1.11	0.29 (0.17)	0.00 (0.00)	1.28 (1.26)	1.02 (1.02)	1.32 (1.40)	1.11 (1.13)
$NbSi_2N_4$	2.97	pn	1.61	1.16	1.76	1.76	1.61	1.21	1.74 (1.74)	1.11 (1.12)	2.07 (2.09)	1.73 (1.77)	1.66 (1.65)	1.27 (1.26)
$NbGe_2N_4$	3.09	pn	1.63	1.04	1.20	1.00	1.29	1.09	1.60 (1.60)	1.04 (1.04)	1.31 (1.31)	1.05 (1.04)	1.41 (1.41)	1.10 (1.10)
$NbSi_2P_4$	3.53	p	0.00	0.00	0.38	0.61	1.76	1.22	0.10 (0.11)	0.00 (0.00)	0.78 (0.80)	0.55 (0.61)	1.59 (1.58)	1.23 (1.22)
$TaSi_2N_4$	2.97	pn	1.70	1.25	1.47	1.52	1.83	1.46	1.93 (1.93)	1.29 (1.29)	1.66 (1.68)	1.42 (1.46)	1.97 (1.96)	1.47 (1.46)
$TaGe_2N_4$	3.08	pn	1.69	1.25	1.02	0.75	1.54	1.17	1.79 (1.78)	1.28 (1.26)	1.02 (1.01)	0.82 (0.81)	1.59 (1.60)	1.18 (1.19)
$TaSi_2P_4$	3.53	p	0.00	0.04	0.18	0.35	1.94	1.48	0.30 (0.32)	0.04 (0.06)	0.49 (0.51)	0.30 (0.36)	1.83 (1.82)	1.49 (1.48)

metal where *GW* and dynamical mean-field theory methods significantly reduce the metallic bandwidth, as demonstrated in Ref. [50]. However, the behavior of energy gaps within the *GW* approximation compared to standard GGA calculations varies across studies. Regarding the HSE06 functional, a recent work [44] reported the effective Coulomb interaction parameters for a broad set of MX_2 (M = Mo, W, Nb, Ta; X = S, Se, Te) compounds across the 1H, 1T, and 1T' phases, finding unconventional Coulomb screening in the 1H structure. This unconventional screening suggests that 2D cold metals do not screen Coulomb interactions as effectively as normal metals, thereby justifying the use of the HSE06 functional for these systems. While *GW* is theoretically more accurate, HSE06 still provides reliable insights into the electronic properties of 2D cold metals.

A. PBE functional

Before presenting our HSE06 and *GW* results, we first validated the consistency of our findings, given that two different codes based on different electronic band structure methods (FLAPW-based FLEUR code and LCAO-based or PW-based QUANTUMATK code) were used, as previously discussed. To ensure reliability, both methods should produce closely matching results for the studied compounds when employing the PBE functional. Table I lists the computed internal and external band gaps (E_g^I and E_g^E), as well as the width of the isolated metallic band (W_m) obtained using the PBE functional with both FLEUR and QUANTUMATK codes. In the later code we employed both the LCAO and PW basis sets (the results using the PW-based QUANTUMATK are presented in parenthesis). While results from FLEUR and QUANTUMATK using the PBE functional show only minor absolute differences, these discrepancies can appear proportionally larger due to the small magnitudes of the values themselves. Similarly, within QUANTUMATK, the chosen basis set (LCAO or PW) also leads to small but observable variations. These findings underscore the sensitivity of numerical results to computational parameters, although among the most recent electronic band structures there is a tendency to produce almost identical results when the same density functional is employed [51]. However, the differences arising from the choice of functional (e.g., PBE versus HSE06) are significantly larger and represent the core focus of this work, as they exert a far more substantial influence on the electronic properties relevant to device applications. This consistency in the absolute values across the different methods employed in our study suggests that the electronic properties derived with PBE are robust and largely unaffected by the choice of the *ab initio* method. Generally, we observe that external band gaps are larger than internal gaps, though they typically remain around 1 eV, while the width of the metallic band is often even greater than both the internal and external energy gaps.

We can use the values of the energy gaps provided in Table I to deduce the cold metal character of each compound when the PBE functional is used. Since the external energy gap is greater than zero for all compounds under study, none is actually an n-type cold metal. Thus, when the internal energy gap is zero, the compound is a p-type cold metal otherwise

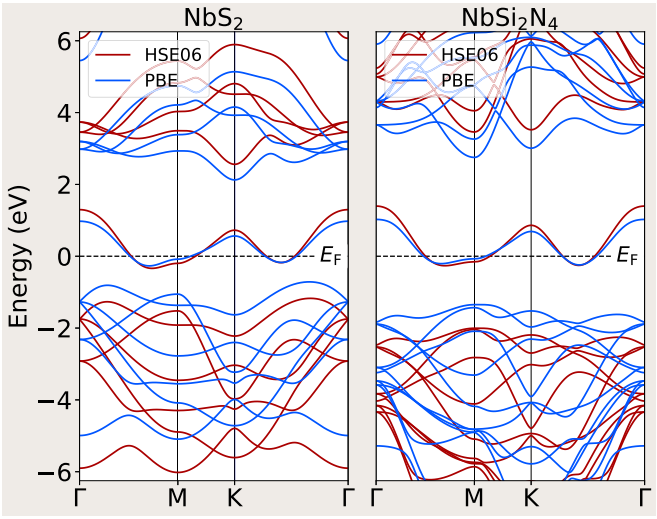

FIG. 4. Band structures of 1H NbS_2 and $NbSi_2N_4$ compounds along high-symmetry lines in the Brillouin zone, calculated using the LCAO-based QUANTUMATK code with both the PBE (blue lines) and HSE06 (red lines) functionals.

it is a pn-type cold metal. The majority of these compounds exhibit a pn-type cold metal character, characterized by an isolated metallic band at the Fermi level that is intersected by the Fermi energy (see Fig. 1). Typical band structures for NbS_2 and $NbSi_2N_4$, calculated using both QUANTUMATK and FLEUR, are shown in Figs. 4 and 5, respectively. As expected from the consistency observed in Table I, both *ab initio* methods yield highly similar band structures under the PBE functional. A defining feature of these band structures is the single, isolated band at the Fermi level, distinctly separated from bands immediately below and above it. This aligns well with findings from Kuc *et al.*, who studied the electronic properties of NbS_2 and other TMDCs, concluding

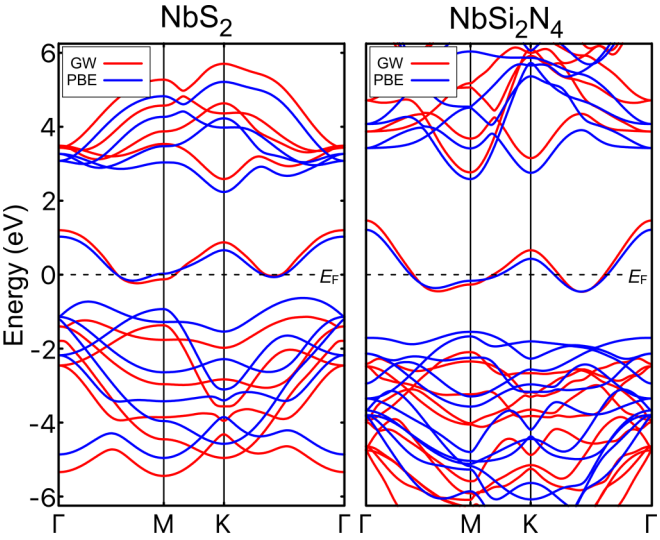

FIG. 5. Band structures of 1H NbS_2 and $NbSi_2N_4$ compounds along high-symmetry lines in the Brillouin zone, calculated using the FLEUR/SPEX code with both the PBE (blue lines) and *GW* approximation (red lines).

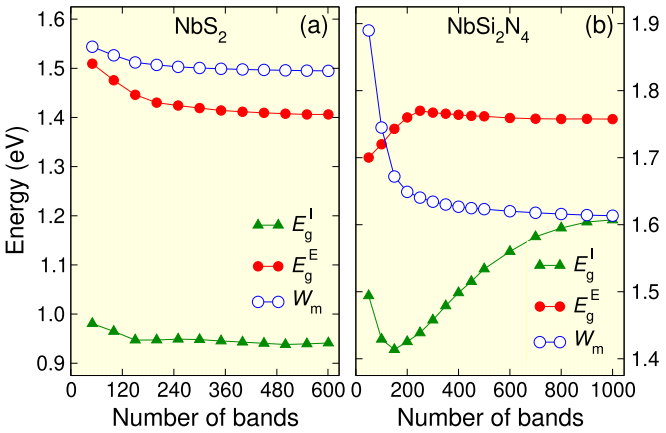

FIG. 6. Dependence of internal and external band gaps (E_g^I and E_g^E), as well as the width W_m of the isolated metallic band, on the number of bands included in the *GW* calculations (a) for NbS_2 and (b) for $NbSi_2N_4$.

that cold metallic behavior is present across its bulk, monolayer, bilayer, and quadrilayer forms [52]. Only a few compounds—$NbTe_2$ and $NbSi_2P_4$—exhibit a p-type cold metal character. $TaTe_2$ is predicted to be a p-type cold metal by QUANTUMATK while FLEUR yields a very small internal energy gap. Finally, we should note that $TaSi_2P_4$ exhibits a very small internal energy gap when PBE is employed, which vanishes when *GW* approximation is used as discussed below.

B. Correlation effects: HSE06 hybrid functional and *GW* approximation

Hybrid functionals like HSE06 are designed to provide a more accurate treatment of the exchange energy than standard GGA functionals, often resulting in an increased band gap in semiconductors. However, the effectiveness of these functionals varies based on material-specific properties due to the mixing coefficients used in combining exact Hartree-Fock and GGA exchange energies. In Ref. [53] $NbSi_2N_4$ was studied using first-principles calculations with the HSE06 functional, revealing a pn-type cold metallic character. The authors showed that the isolated narrow band near the Fermi level is primarily a d_{z^2}-orbital band at the Γ point, centered on the transition metal atoms (Nb). In contrast, the higher occupied valence bands are predominantly *p*-orbital bands from N atoms, while the lower unoccupied conduction bands are mainly derived from *d* orbitals.

Table I presents our calculated results using the HSE06 functional. For all studied materials, HSE06 yields a moderate increase in both the internal and external energy gaps relative to the PBE functional, as expected, along with an increase in the width of the metallic band at the Fermi level. Notably, this effect is more pronounced in the p-type cold metals for which an internal energy gap emerges, classifying these materials as pn-type cold metals under HSE06. Figure 4 compares the HSE06 and PBE band structures using the LCAO-based version of the QUANTUMATK code, illustrating that while HSE06 does not alter the band shapes, it leads to a broader isolated band at the Fermi level and shifts the valence and conduction bands lower and higher in energy, respectively.

Electron correlations are essential in determining the electronic structure of many materials. Although the correlation energy is relatively small—significantly less than the exchange energy and several orders of magnitude smaller than the Hartree energy—it plays a crucial role in accurately describing electronic properties. Therefore, methods like the *GW* approximation are particularly valuable for studying the electronic structure of the materials in our research.

Kim *et al.* have reported the quasiparticle band structure of a monolayer of 1H-$NbSe_2$ using the Quantum Espresso code [54]. Their approach involved a large simulation cell with a carefully converged interlayer distance to minimize interactions between periodic images of the monolayers. Their results showed that the *GW* approximation produced a slightly broader band at the Fermi level compared to the PBE functional and led to significantly larger internal and external band gaps. Similar findings for NbS_2 monolayers were presented in Ref. [55], where *GW* calculations closely matched ARPES experimental data, validating the accuracy of this approach.

The importance of electronic correlations in NbS_2 monolayers was examined by Loon *et al.* [56], who investigated the combined effects of short- and long-range Coulomb interactions and electron–phonon coupling on the material's electronic properties. They found that the interplay of these three interactions generates electronic correlations that differ fundamentally from the effects of each interaction considered independently. The resulting fully interacting electronic spectral function closely resembles the noninteracting band structure but exhibits substantial broadening due to these correlations.

The first step in our *GW* calculations involves ensuring convergence of the electronic band structure with respect to the number of bands included. In Fig. 6, we present convergence tests for two pn-type cold metals, NbS_2 and $NbSi_2N_4$, using a fixed **k**-point grid of $18 \times 18 \times 1$. For NbS_2, both the internal and external band gaps, as well as the width of the isolated metallic band, converge smoothly and rapidly as the number of bands increases, reaching stability within a few meV at approximately 120 bands. In contrast, $NbSi_2N_4$ presents a more challenging case, with the internal gap converging more slowly; achieving similar accuracy requires approximately 800 bands. Based on these findings, we used 600 bands for the MX_2 compounds and 1000 bands for the MA_2Z_4 compounds in our *GW* calculations. Additionally, we performed convergence tests on the **k**-point sampling in the first Brillouin zone, confirming that our chosen grid provides energy gaps and bandwidths with an accuracy of a few meV.

Table I presents the values of the external and internal band gaps, as well as the width of the isolated metallic band at the Fermi level, obtained using the *GW* approximation. As expected, the *GW* method yields larger band gaps and a broader metallic band compared to the PBE functional, exhibiting a trend similar to that observed with the HSE06 hybrid functional. However, there is no consistent pattern in the relative increases in gap values between *GW* and HSE06: in some materials, HSE06 results in a greater increase over PBE, while in others, the *GW* method shows a larger effect. The influence of *GW* on the band structure of pn-type cold metals is illustrated in Fig. 5, where we compare the PBE and *GW* band structures for NbS_2 and $NbSi_2N_4$. It is worth noting that

non-self-consistent one-shot *GW* calculations are known to not conserve the electronic charge, as the Green's function and self-energy are not iteratively updated [57–59]. To address this issue, we used the DFT-PBE band structure as a reference for charge neutrality. Specifically, we applied a uniform energy shift to the *GW*-calculated bands such that their intersection with the Fermi level closely matched the same **k**-points in the Brillouin zone as observed in the DFT-PBE band structure. This procedure ensured the charge neutrality in the *GW* calculations and a consistent reference point for comparing the electronic properties of the materials under study. The *GW* approximation results in a broader metallic band at the Fermi level and simultaneously shifts the valence bands lower and the conduction bands higher in energy, leading to larger internal and external band gaps. Notably, the overall shape of the bands remains similar when comparing the PBE and *GW* band structures. Overall, the impact of *GW* on the PBE band structure resembles the effect observed with the HSE06 functional, as evident from the band structure comparisons in Figs. 4 and 5.

A key distinction between HSE06 and *GW* lies in their treatment of p-type cold metals. As discussed, HSE06 yields a finite internal band gap for all p-type materials in our study, indicating that these materials exhibit pn-type cold metallic behavior. In contrast, the *GW* approximation for $NbTe_2$ and $NbSi_2P_4$ maintains the zero-gap character seen with PBE, thus preserving their p-type cold metallic nature. The behavior of the *GW* approximation with respect to the PBE results, particularly the retention of the zero-gap character in p-type cold metals such as $NbTe_2$ and $NbSi_2P_4$, is expected given that we perform one-shot *GW* calculations. In this approach, *GW* acts as a perturbation to the PBE reference, without iterative updates to the Green's function or self-energy. Consequently, the key characteristics of the PBE band structure are preserved. While fully self-consistent *GW* calculations could potentially provide a more accurate description, they are computationally intensive and beyond the scope of the present study. For $TaSi_2P_4$, *GW* similarly closes the already minimal internal gap found in PBE, reinforcing its intrinsic zero-gap behavior. For $TaTe_2$ *GW* keeps the pn-character observed when FLEUR in conjunction with PBE is employed. This discrepancy likely arises because HSE06 parameters are optimized primarily for semiconductors, limiting its general applicability across all material types. By contrast, *GW* is a more universal approximation, treating correlation effects consistently across materials without altering their fundamental character.

C. Implications for device applications

The implications of our findings for electronic device applications are significant, particularly for the design of NDR tunnel diodes and steep-slope FETs. Among the 2D cold metals we investigated, some have already demonstrated potential as electrode materials in device simulations. In NDR tunnel diodes, three key electronic structure parameters—namely, the internal band gap (E_g^I), external band gap (E_g^E), and metallic bandwidth (W_m)—are crucial in determining the device's *I-V* characteristics and the PVCR value. To achieve a high PVCR in an N-type NDR effect, it is desirable that the metallic bandwidth W_m is smaller than both band gaps. If this condition is not met, then PVCR may be significantly reduced. In MX_2 compounds, our *GW* approximation results reveal substantial increases in band gaps, especially for the internal gap. Despite this enhancement, the metallic bandwidth remains large. For instance, in NbS_2 and $TaSe_2$, W_m exceeds both E_g^I and E_g^E (i.e., $W_m > E_g^E > E_g^I$), whereas, in $NbSe_2$ and $TaSe_2$, the external gap E_g^E is greater than W_m, followed by the internal gap ($E_g^E > W_m > E_g^I$). The latter group is anticipated to produce an N-type NDR effect with moderate PVCR values when used as electrodes in tunnel diodes, while the former group may yield lower PVCR values. In particular, $NbSi_2N_4$ emerges as a highly promising material for NDR tunnel diode applications, satisfying the ideal condition of $E_g^E > E_g^I > W_m$. Prior studies (Ref. [19]) have explored lateral NDR tunnel diodes based on $NbSi_2N_4$ electrodes, where DFT combined with nonequilibrium Green's function (NEGF) simulations at the PBE level reported an impressively high PVCR of 10^3-10^5. Notably, at the PBE level, the internal band gap of $NbSi_2N_4$ is smaller than its bandwidth. Other materials in this group, such as $NbGe_2N_4$ and $TaSi_2N_4$, also hold promise, as indicated in Table I.

For FET applications, the critical parameters are the external band gap and the bandwidth W_m^E above the Fermi level (often referred to as the valence band maximum in p-type cold metals). A larger external band gap combined with a smaller bandwidth W_m^E enhances the filtering of high-energy hot electrons in FETs, enabling subthreshold slopes below the thermionic limit of 60 mV/dec at room temperature. Recent studies have demonstrated sub-60 mV/dec SS values in FETs with cold metal electrodes like NbS_2, TaS_2, and $NbTe_2$ using the DFT + NEGF method at the PBE level [28]. When correlation effects are incorporated in device simulations, similar subthreshold swings may be anticipated. However, while the increased external band gap due to correlations is beneficial, it may be counterbalanced by the concurrent increase in W_m^E, which could slightly reduce the efficiency of hot electron filtering. These insights underscore the promise and challenges of using 2D cold metals in advanced nanoelectronic devices, where a nuanced understanding of correlation effects is essential for optimizing device performance.

V. SUMMARY AND CONCLUSIONS

In this work, we investigated the influence of correlation effects on the electronic band structure of 2D cold metals MX_2 and MA_2Z_4 (M = Nb, Ta; X = S, Se, Te; A = Si, Ge; Z = N, P) using the *GW* approximation and HSE06 hybrid functional. These cold metals, characterized by their unique electronic features—namely, an isolated metallic band near the Fermi level with distinct internal and external band gaps—show substantial promise for use in advanced nanoelectronic devices, such as NDR tunnel diodes and FETs with steep subthreshold slopes. Our results indicate that both *GW* and HSE06 enhance the internal (E_g^I) and external (E_g^E) band gaps and, to a lesser extent, the width of the metallic band (W_m). However, the internal band gap E_g^I displays the greatest sensitivity to correlation effects, underscoring its importance in determining the electronic characteristics of these materials. These three

band structure parameters are essential for optimizing the performance of cold metal-based devices.

For NDR tunnel diodes, our findings suggest that materials like NbSi2N_4, with an ideal band structure hierarchy ($E_g^E > E_g^I > W_m$), are particularly suited for achieving high PVCR values. Other compounds, such as $NbGe_2N_4$ and $TaSi_2N_4$, also show promising band structures conducive to NDR applications, with moderate PVCR values expected based on the band hierarchy. For FET applications, we highlight that a large external band gap combined with a narrow bandwidth above the Fermi level supports efficient hot-electron filtering, which is necessary to achieve sub-60 mV/dec subthreshold swings at room temperature. Our study suggests that incorporating correlation effects in device simulations may reveal an improved capability for subthreshold performance, although the increased metallic bandwidth may present challenges for optimizing hot-electron filtering. Our findings provide a robust theoretical foundation for the use of 2D cold metals in nanoelectronic applications, where understanding and leveraging correlation effects is crucial. This work opens avenues for further experimental and theoretical research aimed at enhancing the design of cold metal-based devices, paving the way for next-generation electronics with superior performance metrics in both switching speed and energy efficiency.

ACKNOWLEDGMENTS

This work was supported by the European Union (EFRE) via Grant No: ZS/2016/06/79307, the Federal Ministry of Education and Research of Germany (BMBF) in the framework of the Palestinian-German Science Bridge (BMBF Grant No. DBP01436), and the Deutsche Forschungsgemeinschaft (DFG) through the Collaborative Research Center SFB 1238 (Project C01) and SFB/TRR 227. M.T. acknowledges the TUBITAK ULAKBIM, High Performance and Grid Computing Center (TRUBA resources).

DATA AVAILABILITY

The data supporting this study's findings are available within the article.

[1] A. H. Castro Neto, F. Guinea, N. M. R. Peres, K. S. Novoselov, and A. K. Geim, The electronic properties of graphene, Rev. Mod. Phys. **81**, 109 (2009).

[2] Z. Zhang, M. Yang, P. Hong, S. Jiang, G. Zhao, J. Shi, Q. Xie, and Y. Zhang, Recent progress in the controlled synthesis of 2D metallic transition metal dichalcogenides, Nanotechnology **30**, 182002 (2019).

[3] P. Kumbhakar, J. S. Jayan, A. S. Madhavikutty, P. R. Sreeram, A. Saritha, T. Ito, and C. S. Tiwary, Prospective applications of two-dimensional materials beyond laboratory frontiers: A review, iScience **26**, 106671, (2023).

[4] M. Zeng, Y. Xiao, J. Liu, X. Yang, and L. Fu, Exploring two-dimensional materials toward the next-generation circuits: From monomer design to assembly control, Chem. Rev. **118**, 6236 (2018).

[5] V. Shanmugam, R. A. Mensah, K. Babu, S. Gawusu, A. Chanda, Y. Tu, R. E. Neisiany, M. Försth, G. Sas, and O. Das, A review of the synthesis, properties, and applications of 2D materials, Part. Part. Syst. Charact. **39**, 2200031 (2022).

[6] A. K. Singh, P. Kumbhakar, A. Krishnamoorthy, A. Nakano, K. K. Sadasivuni, P. Vashishta, A. K. Roy, V. Kochat, and C. S. Tiwary, Review of strategies toward the development of alloy two-dimensional (2D) transition metal dichalcogenides, iScience **24**, 103532 (2021).

[7] F. Ricci, A. Dunn, A. Jain, G.-M. Rignanese, and G. Hautier, Gapped metals as thermoelectric materials revealed by high-throughput screening, J. Mater. Chem. A **8**, 17579 (2020).

[8] M. R. Khan, H. R. Gopidi, and O. I. Malyia, Optical properties and electronic structures of intrinsic gapped metals: Inverse materials design principles for transparent conductors, Appl. Phys. Lett. **123**, 061101 (2023).

[9] O. I. Malyi and A. Zunger, False metals, real insulators, and degenerate gapped metals, Appl. Phys. Rev. **7**, 041310 (2020).

[10] L. Zhang and F. Liu, High-throughput approach to explore cold metals for electronic and thermoelectric devices, npj Comput. Mater. **10**, 78 (2024).

[11] J. B. Khurgin and G. Sun, In search of the elusive lossless metal, Appl. Phys. Lett. **96**, 181102 (2010).

[12] M. N. Gjerding, M. Pandey, and K. S. Thygesen, Band structure engineered layered metals for low-loss plasmonics, Nat. Commun. **8**, 15133 (2017).

[13] F. H. da Jornada, L. Xian, A. Rubio, and S. G. Louie, Universal slow plasmons and giant field enhancement in atomically thin quasi-two-dimensional metals, Nat. Commun. **11**, 1013 (2020).

[14] C. Song, X. Yuan, C. Huang, S. Huang, Q. Xing, C. Wang, C. Zhang, Y. Xie, Y. Lei, F. Wang *et al.*, Plasmons in the van der Waals charge-density-wave material 2H-$TaSe_2$, Nat. Commun. **12**, 386 (2021).

[15] H. Gao, C. Ding, J. Son, Y. Zhu, M. Wang, Z. G. Yu, J. Chen, L. Wang, S. A. Chambers, T. W. Noh *et al.*, Ultra-flat and long-lived plasmons in a strongly correlated oxide, Nat. Commun. **13**, 4662 (2022).

[16] H. Yu, Y. Peng, Y. Yang, and Z.-Y. Li, Plasmon-enhanced light–matter interactions and applications, npj Comput. Mater. **5**, 45 (2019).

[17] E. Şaşıoğlu and I. Mertig, Theoretical prediction of semiconductor-free negative differential resistance tunnel diodes with high peak-to-valley current ratios based on two-dimensional cold metals, ACS Appl. Nano Mater. **6**, 3758 (2023).

[18] Y. Yin, C. Shao, H. Guo, J. Robertson, Z. Zhang, and Y. Guo, Negative differential resistance effect in "cold" metal heterostructure diodes, IEEE Electron Device Lett. **43**, 498 (2022).

[19] P. Bodewei, E. Şaşıoğlu, N. F. Hinsche, and I. Mertig, Computational design of tunnel diodes with negative differential resistance and ultrahigh peak-to-valley current ratio based on two-dimensional cold metals: The case of $NbSi_2N_4/HfSi_2N_4/NbSi_2N_4$ lateral heterojunction diode, Phys. Rev. Appl. **22**, 014004 (2024).

[20] A. L. Efros, Density of states and interband absorption of light in strongly doped semiconductors, Sov. Phys. Usp. **16**, 789 (1974).

[21] P. K. Chakraborty and K. P. Ghatak, On the density-of-states function in heavily doped compound semiconductors, Phys. Lett. A **288**, 335 (2001).

[22] E. O. Kane, Band tails in semiconductors, Solid-State Electron. **28**, 3 (1985).

[23] P. Van Mieghem, Theory of band tails in heavily doped semiconductors, Rev. Mod. Phys. **64**, 755 (1992).

[24] S. Sant and A. Schenk, The effect of density-of-state tails on band-to-band tunneling: Theory and application to tunnel field effect transistors, J. Appl. Phys. **122**, 135702 (2017).

[25] J. Bizindavyi, A. S. Verhulst, Q. Smets, D. Verreck, B. Sorée, and G. Groeseneken, Band-tails tunneling resolving the theory-experiment discrepancy in Esaki diodes, IEEE J. Electron Devices Soc. **6**, 633 (2018).

[26] A. Schenk and S. Sant, Tunneling between density-of-state tails: Theory and effect on Esaki diodes, J. Appl. Phys. **128**, 014502 (2020).

[27] Z. Wang, X. Xie, L. Zhang, R. Cao, X. Liu, S. Cho, and F. Liu, Cold source diodes with sub-unity ideality factor and giant negative differential resistance, IEEE Electron Device Lett. **43**, 2184 (2022).

[28] F. Liu, Switching at less than 60 mV/Decade with a "cold" metal as the injection source, Phys. Rev. Appl. **13**, 064037 (2020).

[29] C. Qiu, F. Liu, L. Xu, B. Deng, M. Xiao, J. Si, L. Lin, Z. Zhang, J. Wang, H. Guo *et al.*, Dirac-source field-effect transistors as energy-efficient, high-performance electronic switches, Science **361**, 387 (2018).

[30] Z. Tang, C. Liu, X. Huang, S. Zeng, L. Liu, J. Li, Y.-G. Jiang, D. W. Zhang, and P. Zhou, A steep-slope MoS_2/graphene Dirac-source field-effect transistor with a large drive current, Nano Lett. **21**, 1758 (2021).

[31] Y. Xiao, M. Zhou, J. Liu, J. Xu, and L. Fu, Phase engineering of two-dimensional transition metal dichalcogenides, Sci. China Mater. **62**, 759 (2019).

[32] Y. Xiao, C. Xiong, M.-M. Chen, S. Wang, L. Fu, and X. Zhang, Structure modulation of two-dimensional transition metal chalcogenides: Recent advances in methodology, mechanism and applications, Chem. Soc. Rev. **52**, 1215 (2023).

[33] L. Wang, Y. Shi, M. Liu, A. Zhang, Y.-L. Hong, R. Li, Q. Gao, M. Chen, W. Ren, H.-M. Cheng, Y. Li, and X.-Q. Chen, Intercalated architecture of MA_2Z_4 family layered van der Waals materials with emerging topological, magnetic and superconducting properties, Nat. Commun. **12**, 2361 (2021).

[34] Y. L. Hong, Z. B. Liu, L. Wang, T. Y. Zhou, W. Ma, C. X, S. Feng, L. Chen, M. L. Chen, D. M. Sun, X. Q. Chen, H. M. Cheng, and W. C. Ren, Chemical vapor deposition of layered two-dimensional $MoSi_2N_4$ materials, Science **369**, 670 (2020).

[35] M. N. Gjerding, A. Taghizadeh, A. Rasmussen, S. Ali, F. Bertoldo, T. Deilmann, U. P. Holguin, N. R. Knøsgaard, M. Kruse, A. H. Larsen, S. Manti, T. G. Pedersen, T. Skovhus, M. K. Svendsen, J. J. Mortensen, T. Olsen and K. S. Thygesen, Recent Progress of the Computational 2D Materials Database (C2DB), 2D Materials **8**, 044002 (2021).

[36] F. A. Rasmussen and K. S. Thygesen, Computational 2D materials database: Electronic structure of transition-metal dichalcogenides and oxides, J. Phys. Chem. C **119**, 13169 (2015).

[37] S. Haastrup, M. Strange, M. Pandey, T. Deilmann, P. S. Schmidt, N. F. Hinsche, M. N. Gjerding, D. Torelli, P. M. Larsen, A. C. Riis-Jensen, J. Gath, K. W. Jacobsen, J. J. Mortensen, T. Olsen, and K. S. Thygesen, The computational 2D materials database: Highthroughput modeling and discovery of atomically thin crystals, 2D Mater. **5**, 042002 (2018).

[38] S. Smidstrup, D. Stradi, J. Wellendorff, P. A. Khomyakov, U. G. Vej-Hansen, M.-E. Lee, T. Ghosh, E. Jónsson, H. Jónsson, and K. Stokbro, First-principles Green's-function method for surface calculations: A pseudopotential localized basis set approach, Phys. Rev. B **96**, 195309 (2017).

[39] S. Smidstrup, T. Markussen, P. Vancraeyveld, J. Wellendorff, J. Schneider, T. Gunst, B. Verstichel, D. Stradi, P. A. Khomyakov, U. G. Vej-Hansen, M.-E. Lee, S. T. Chill, F. Rasmussen, G. Penazzi, F. Corsetti, A. Ojanpera, K. Jensen, M. L. N. Palsgaard, U. Martinez, A. Blom *et al.*, QuantumATK: An integrated platform of electronic and atomic-scale modelling tools, J. Phys.: Condens. Matter **32**, 015901 (2020).

[40] M. J. van Setten, M. Giantomassi, E. Bousquet, M. J. Verstraete, D. R. Hamann, X. Gonze, and G. M. Rignanese, The PSEUDODOJO: Training and grading a 85 element optimized norm-conserving pseudopotential table, Comput. Phys. Commun. **226**, 39 (2018).

[41] J. P. Perdew, K. Burke, and M. Ernzerhof, Generalized gradient approximation made simple, Phys. Rev. Lett. **77**, 3865 (1996).

[42] J. Heyd, G. E. Scuseria, and M. Ernzerhof, Hybrid functionals based on a screened Coulomb potential, J. Chem. Phys. **118**, 8207 (2003).

[43] J. Heyd, G. E. Scuseria, and M. Ernzerhof, Erratum: "Hybrid functionals based on a screened Coulomb potential" [J. Chem. Phys. 118, 8207 (2003)], J. Chem. Phys. **124**, 219906 (2006).

[44] H. R. Ramezani, E. Şaşıoğlu, H. Hadipour, H. R. Soleimani, C. Friedrich, S. Blügel, and I. Mertig, Nonconventional screening of Coulomb interaction in two-dimensional semiconductors and metals: A comprehensive constrained random phase approximation study of MX_2 (M = Mo, W, Nb, Ta; X = S, Se, Te), Phys. Rev. B **109**, 125108 (2024).

[45] H. J. Monkhorst and J. D. Pack, Special points for Brillouin-zone integrations, Phys. Rev. B **13**, 5188 (1976).

[46] D. Wortmann, G. Michalicek, N. Baadji, M. Betzinger, G. Bihlmayer, I. Bröder, T. Burnus, J. Enkovaara, F. Freimuth, C. Friedrich, C.-R. Gerhorst, S. Granberg Cauchi, U. Grytsiuk, A. Hanke, J.-P. Hanke, M. Heide, S. Heinze, R. Hilgers, H. Janssen, D. A. Klüppelberg, R. Kovacik, P. Kurz, M. Lezaic, G. K. H. Madsen, Y. Mokrousov, A. Neukirchen, M. Redies, S. Rost, M. Schlipf, A. Schindlmayr, M. Winkelmann, S. Blügel, "FLEUR (MaX-R7.2)", Zenodo (2024), doi:10.5281/zenodo.13833162.

[47] C. Friedrich, S. Blügel, and A. Schindlmayr, Efficient implementation of the *GW* approximation within the all-electron FLAPW method, Phys. Rev. B **81**, 125102 (2010).

[48] C. Friedrich, M. C. T. D. Müller, J. Kirchmair, R. Sakuma, E. Sasioglu, M. Niesert, and S. Blügel, "Spex code", Zenodo (2023), doi: 10.5281/zenodo.14017762.

[49] T. Kotani and M. van Schilfgaarde, All-electron *GW* approximation with the mixed basis expansion based on the full-potential LMTO method, Solid State Commun. **121**, 461 (2002).

[50] R. Sakuma, P. Werner, and F. Aryasetiawan, Electronic structure of $SrVO_3$ within *GW*+DMFT, Phys. Rev. B **88**, 235110 (2013).

[51] K. Lejaeghere, G. Bihlmayer, T. Björkman, P. Blaha, S. Blügel, V. Blum, D. Caliste, I. E. Castelli, St. J. Clark, A. D. Corso,

S. de Gironcoli, T. Deutsch, J. K. Dewhurst, I. Di Marco, C. Draxl, M. Dułak, O. Eriksson, J. A. Flores-Livas, K. F. Garrity, L. Genovese *et al.*, Reproducibility in density-functional theory calculations of solids, Science **351**, aad3000 (2016).

[52] A. Kuc, N. Zibouche, and T. Heine, Influence of quantum confinement on the electronic structure of the transition metal sulfide TS_2, Phys. Rev. B **83**, 245213 (2011).

[53] M. R. K. Akanda and R. K. Lake, Magnetic properties of $NbSi_2N_4$, VSi_2N_4, and VSi_2P_4 monolayers, Appl. Phys. Lett. **119**, 052402 (2021).

[54] S. Kim and Y.-W. Son, Quasiparticle energy bands and Fermi surfaces of monolayer $NbSe_2$, Phys. Rev. B **96**, 155439 (2017).

[55] C. Heil, M. Schlipf, and F. Giustino, Quasiparticle *GW* band structures and Fermi surfaces of bulk and monolayer NbS_2, Phys. Rev. B **98**, 075120 (2018).

[56] E. G. C. P. van Loon, M. Rösner, G. Schönhoff, M. I. Katsnelson, and T. O. Wehling, Competing Coulomb and electron–phonon interactions in NbS_2, npj Quantum Mater. **3**, 32 (2018).

[57] A. Schindlmayr, P. García-González, and R. W. Godby, Diagrammatic self-energy approximations and the total particle number, Phys. Rev. B **64**, 235106 (2001).

[58] F. Aryasetiawan and O. Gunnarsson, The *GW* method, Rep. Prog. Phys. **61**, 237 (1998).

[59] G. Onida, L. Reining, and A. Rubio, Electronic excitations: Density-functional versus many-body Green's-function approaches, Rev. Mod. Phys. **74**, 601 (2002).